

A Short review of material synthesizing process by using ultrasonic method and photocatalytic hydrogen evolution via water splitting

Md Nazmodduha Rafat and Won-Chun Oh*

**Department of Advanced Materials Science & Engineering, Hanseo University, Seosan-si, Chungnam, Korea*

Abstract: Sonochemistry is the implementation of ultrasound wave to chemical reactions and processes. Remarkable progress has been achieved over the years on ultrasonic process for novel material synthesis. Nanostructured materials have attracted much attention in recent decades. Nowadays, there are numerous nanomaterials with several applications. Photocatalytic H₂ generation via water splitting is increasingly gaining attention as a viable alternative for improving the performance of H₂ production for solar energy conversion. Many methods were developed to enhance photocatalyst efficiency, primarily by modifying its morphology, crystallization, and electrical properties. Here, we summarize recent achievements in the synthesis and application of various photocatalysts. The rational design of novel photocatalysts was achieved using various strategies, and the applications of novel materials for H₂ production are displayed herein. Meanwhile, the challenges and prospects for the future development of H₂-producing photocatalysts are also summarized.

Key words: Ultra sonication, photocatalyst, water splitting, nano-material, hydrogen.

Introduction

The development of renewable green energy sources is a critical challenge for modern society. H₂ is environmentally friendly, renewable, and considered to be an ideal candidate for an economically and socially sustainable fuel [1–6], and was previously regarded as an alternative energy source. Interestingly, some researchers also found that H₂-rich water has neuron effects owing to its antioxidant properties. Although the deep mechanism is not clear, more and more researchers made an effort to study the biological function of H₂ [7–21]. To date, almost all H₂ gas production processes in the industry are based on natural gas, coal, petroleum, or water electrolysis. These traditional preparation methods are limited due to the associated CO₂ emissions and high energy consumption. Hence, it is urgent to develop a low-cost method for efficient H₂ generation and, thus, support the emerging H₂ economy. The sun provides an energy output of ~3 10²⁴ J per year, which is approximately 12,000 times higher than the current energy demand. Therefore, solar energy can act as a sustainable alternative energy source in the future. To date, the transformation of solar energy into H₂ via water splitting is deemed as a

desirable H₂ preparation method to solve the energy crisis [22,23]. The proper use of H₂ requires insight into the physical properties of H₂ molecules. As we know, the lengths and strengths of hydrogen bonds are exquisitely sensitive to temperature and pressure. Meanwhile, the charges of H₂ molecules also vary with temperature [24] because the spin direction of the nucleus in the H₂ molecule changes depending on the temperature, and an energy difference occurs between H₂ molecules. The para-H₂ fraction changes with temperature, and it is necessary to understand the characteristics of H₂ molecules according to temperature [25]. During the reaction, hydrogen can be used safely at room temperature; however, it is rather dangerous in high-temperature environments. As we know, H₂ gas, often called dihydrogen or molecular H₂, is a highly flammable gas with a wide range of concentrations between 4% and 75% by volume. Meanwhile, H₂ is the world's lightest gas. The density of H₂ is only 1/14 of that of air. At 0° C, the density of H₂ is only 0.0899 g/L at standard atmospheric pressure, which is the smallest-molecular-weight substance; it is mainly used as a reducing agent. It has various applications in the petrochemical, electronic, and metallurgical industry, as well as in food processing, float glass, fine organic synthesis, aerospace, and other fields. At the same time, H₂ is also an ideal secondary energy source. Owing to the properties of H₂, the aerospace industry uses liquid H₂ as fuel. Now, it is common to produce H₂ from water gas rather than using high energy-consuming water. The produced H₂ is used in large quantities in the cracking reaction of the petrochemical industry and the production of ammonia. Unfortunately, all H₂ production methods are highly energy (thermal and electrical) demanding, which limits their application. Thus, it is crucial to find a new method of H₂ production. Fujishima and Honda first reported photocatalytic water splitting using a TiO₂ electrode in 1972 [26]. Research on solar H₂ production attracted researchers in various fields, such as (1) chemists for the design and synthesis of various catalysts to investigate structure–property relationships; (2) physicists to fabricate semiconductor photocatalysts with novel electronic structures, as predicted by theoretical calculation; and (3) material scientists to construct unique photocatalytic materials with novel structures and morphologies [27–30]. When photocatalysts are illuminated at wavelengths which are suitable to their band gap energy, after the excitation, the charge carriers will either combine or transfer to the surface of the photocatalysts to participate in photocatalytic reactions. For the generation of efficient semiconductor photocatalysts, long-lived charge carriers and high stability are required [31–33]. Significant developments were made toward H₂ generation via water splitting over the last several decades by a number of talented researchers [34–38]. Herein, we attempt to sum up the advances achieved to date. Therefore, we briefly summarize the background related to various photocatalysts for H₂ generation and the achievements of high-efficiency photocatalysts. The main synthesis routes and modifications for adjusting the band structure to harvest light and enhance charge separation are also discussed.

In the pioneering study by Fujishima and Honda [27], electrochemical cells were made up for the splitting of the water into H₂ and O₂, as shown in Fig. 1. While the TiO₂ electrode was under ultraviolet (UV) light irradiation, water oxidation (oxygen evolution) occurred on its surface, while the reduction reaction (H₂ evolution) occurred on the

surface platinum black electrode. With this study in mind, semiconductor photocatalysts were later developed by Bard et al. in their design of a novel photocatalytic system.

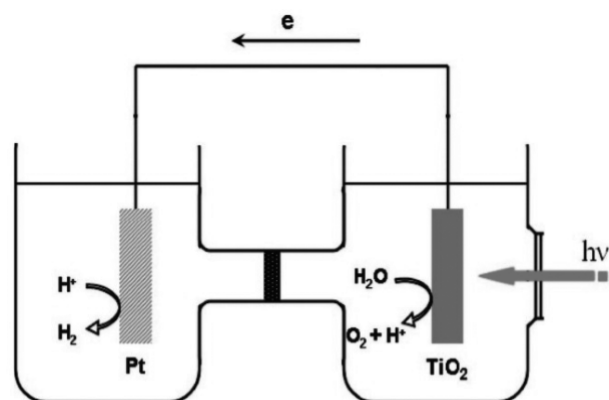


Fig. 1. Schematic of a photoelectrochemical cell (PEC).

Fig. 2a shows a display of hydrogen evolution by photocatalysts. The photocatalytic reaction occurring on the semiconductor photocatalysts can be divided into three parts: (1) obtaining photons with energy exceeding that of the photocatalysts band gap, generating electron and hole pairs; (2) separating carriers by migration in the semiconductor photocatalyst; and (3) reaction between these carriers and H_2O [39–46]. In addition, electron–hole pairs will combine with each other simultaneously. As shown in Fig. 2b, while photocatalysts are involved in hydrogen evolution, the lowest position of the conduction band (CB) should be lower than the reduction position of $\text{H}_2\text{O}/\text{H}_2$, while the position of the valence band (VB) should be higher than the potential of $\text{H}_2\text{O}/\text{O}_2$ [47–50].

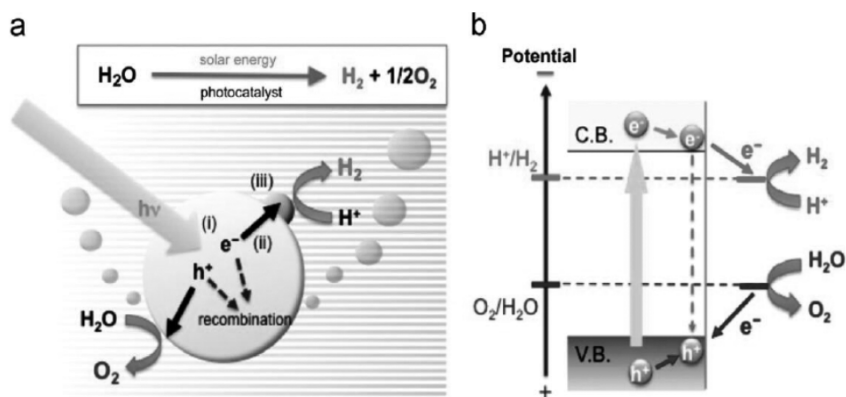


Fig. 2. Schematic illustration of hydrogen evolution over photocatalysts.

Experimental Description

Many photocatalysts were created as photocatalysts for hydrogen evolution. Based on these species, they can be divided into three major parts: (1) graphene-based photocatalyst; (2) graphitic carbon nitride ($g\text{-C}_3\text{N}_4$)-based photocatalysts; and (3) heterojunction photocatalysts (semiconductor - semiconductor or semiconductor-(metal, element)).

Recently, graphene-based photocatalysts attracted significant attention for enhancing photocatalytic H_2 production performance. Graphene is used to enhance photocatalytic efficiency owing to its novel structure and electrochemical properties (Fig. 3). Fig. 3. Proposed mechanism of graphene-based photocatalysts. Reproduced with permission from Reference [56]; American Chemical Society. To date, many reports regarding the synthesis of graphene-based photocatalysts with improved photocatalytic efficiency were published. Graphene is a well-known two-dimensional (2D) material, which can improve surface area, and its 2D membrane-like structure imparts unique electrochemical properties [57–60]. Generally speaking, photocatalysts prepared by simple physical mixing with graphene will involve only a bit of direct contact with the graphene sheets. This small amount of contact between the photocatalyst and graphene results in weak interactions and inhibits charge transfer rates. Hence, the synthesis of photocatalysts with more interactions is highly needed. Previously, Kim et al. synthesized novel graphene oxide (GO)- TiO_2 photocatalysts [58] in 2013, comprising a core-shell nanostructure with enhanced photocatalytic efficiency (Fig. 4). The improved H_2 production activity compared to that of TiO_2 revealed that the utilization of the core-shell structure enhanced photocatalytic efficiency. This novel structural design offers three dimensional (3D) close contact between the materials and provides more active sites, which will enhance the charge separation rate and H_2 production efficiency [61–63].

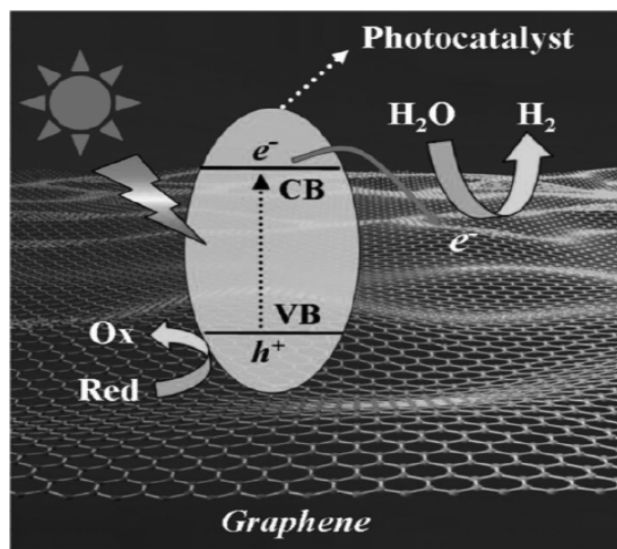


Fig. 3. Proposed mechanism of graphene-based photocatalysts.

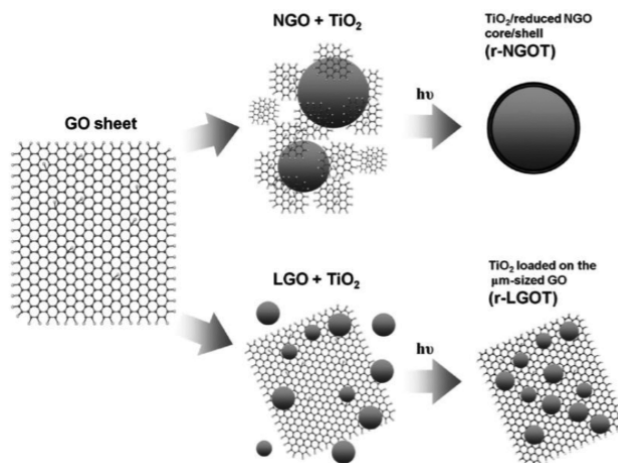


Fig. 4. Schematic display of synthetic process of graphene oxide (GO)/TiO₂ and TiO₂/GO.

Currently, many researchers are more interested in visible-light-driven photocatalysts, which are achieved using band-gap modification or taking graphene as a photosensitizer to broaden the visible-light adsorption range [64–66]. Significant efforts were conducted for building visible-light response systems because of the UV-only response of TiO₂, and its nontoxic properties [67]. Recently, it was found that graphene regulating TiO₂ involves visible-light adsorption activity. The carbon layered structure of graphene with enriched δ electrons forms bonds with titanium atoms. As a result, this strong interaction will shift the band position and reduce the band gap [68–70]. Lee et al. [71] also achieved a lower band gap using a graphene/TiO₂ photocatalyst. The improved photocatalytic efficiency of the graphene/TiO₂ composite owes to the band-gap regulation, which consequently promotes charge transfer rates through the graphene sheet.

Currently, carbon-nitride-based photocatalysts receive significant attention for their photocatalytic H₂ generation owing to a unique electronic structure (Fig. 5) [72–77]. This section summarizes recent significant achievements in building C₃N₄-based photocatalysts for H₂ evolution. Methods including nanostructure regulation, band-gap modification, dye sensitization, and heterojunction fabrication are highlighted herein. Recently, carbon nitride attracted significant attention following the pioneering research of Wang et al. in 2009 for photocatalytic hydrogen evolution [78,79]. The assumed structure of C₃N₄ is a 2D framework with the tri-s-thiazine linked by tertiary amines (Fig. 6); it is thermally stable and chemically stable. Pioneering studies regarded g-C₃N₄ as a visible-light-driven photocatalyst with a band gap of approximately 2.7 eV and an appropriate band position for water splitting [80–85]. Hence, g-C₃N₄ is an ideal candidate for photocatalytic H₂ evolution.

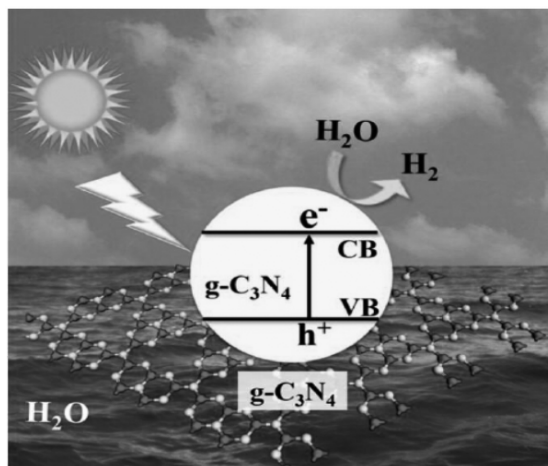


Fig. 5. Proposed mechanism of graphitic carbon nitride (g-C₃N₄)-based photocatalysts.

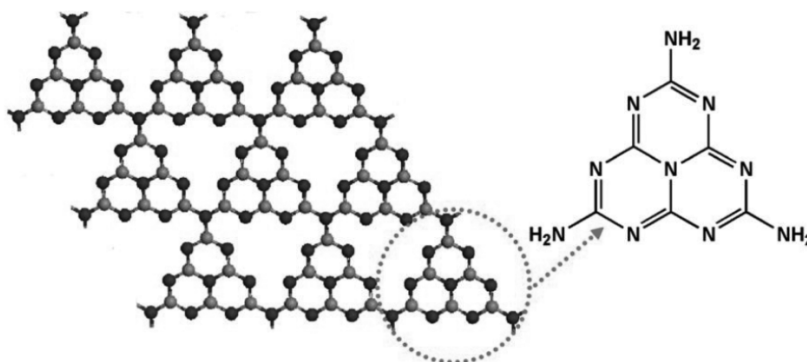


Fig. 6. Schematic display of the structure of g-C₃N₄.

Metal loading is also regarded as a useful method for photocatalytic enhancement. Song et. al. [86] constructed Ag-rGO-TiO₂ composite photocatalysts (Fig. 7) in 2018. In order to analyze the photocatalytic mechanism of the architectural Ag-TiO₂ and Ag-rGO-TiO₂ composites, their structures with Ag nanocubes for light absorption and TiO₂ nanosheets were well displayed. The difference between Ag-TiO₂ and Ag-rGO-TiO₂ is the interface between Ag nanocubes and TiO₂ nanosheets, which enhances the electron transfer capability. For Ag-TiO₂, the direct contact between the two materials results in the formation of Ag (100)/(001) TiO₂ interface. Meanwhile, for Ag-rGO-TiO₂, both Ag(100)/rGO and rGO/(001) TiO₂ interfaces are formed by rGO. As mentioned above, the synergistic effect of Ag(100)/rGO and rGO/(001)TiO₂ interfaces, rather than the Ag(100)/(001) TiO₂ interface, offers quicker electron transfer. As shown in Fig. 7, no Schottky barrier is formed between Ag and TiO₂, and the hot electrons on the surface of TiO₂ flow back to Ag and then recombine with holes. Meanwhile, for the Ag rGO-TiO₂

sample, no barrier is necessary to facilitate the electron transfer. The electrons generated on the surface of Ag nanocubes with smaller work function flow to rGO via a contact so as to equilibrate the electron Fermi distribution on the interface [87,88]. Moreover, the rGO nanosheets can act as conductive channels, further transferring the electron to the rGO/TiO₂ interface. Owing to the light absorption of rGO, the transferred electrons within the rGO nanosheets can be further transferred to the CB of TiO₂ under light excitation. The proposed photocatalytic mechanism of Ag-rGO-TiO₂ illustrated in Fig. 7.

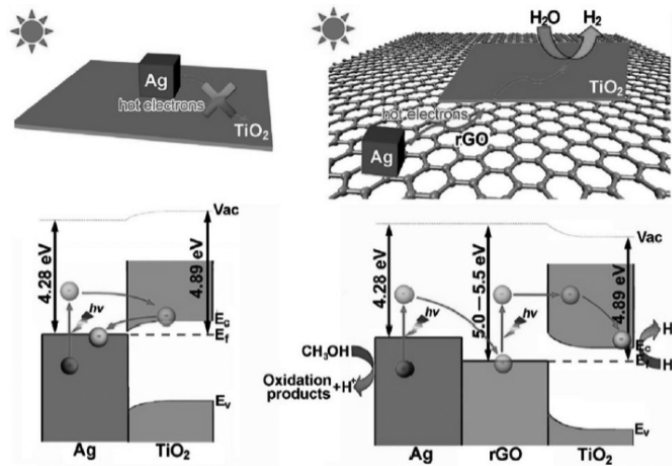


Fig. 7. Schematic illustrating photocatalytic mechanism for Ag-TiO₂ and Ag-rGO-TiO₂ samples under visible-light irradiation.

4. Result and discussion

To have a first evaluation of influence of various amounts of CdSe-graphene (CG) as well as influence of different surfactant sources and its transformation to various samples of SiO₂/CdSe-graphene (SCG) nanocomposites, the X-ray diffraction (XRD, Shimadzu XD-D1) of SCG nanocomposites were recorded to determine component crystalline phase information of particles, shown in Fig. 8. They were four similar features of all survey composites achieved from XRD patterns. First, all diffraction peaks were clear without unexpected peaks and baselines were smoothing with a narrow width that confirmed purity of materials. Second, the XRD pattern displayed the same main typical diffraction signals at $2\theta = 25.5^\circ$, 42.2° and 49.8° belonging to diffractions of (111), (220) and (311) plane well-indexed to cubic crystal structure CdSe according to standard power diffraction data (JCPDS No. 65-2891 for CdSe, cubic) [89,90]. Third, presence of a silica signal with a broad diffraction peak at 2θ of 22.9° were attended [91,92]. What is more, in the case of the CG and TEOS mass ratios of 5:100 (SCG-1, and SCG-A), silica peak with dominant effect overlapped low diffraction peak of the CdSe signal. In the opposite direction, when increasing mass ratios of CG in the SCG nanocomposites, diffraction peaks of CdSe became dominant with more diffraction signals at $2\theta = 21.9^\circ$, 24.0° , 25.5° , 27.1° , 31.8° , 36.0° , 42.2° , 46.1° , 49.8° and 57.0° implying presence of CdSe in large amounts in nanocomposites. The last point, no graphene peaks were recorded in

XRD patterns of all survey nanocomposites because of dominant effect of silica. The reason was that fixation of SiO_2 particles onto the surface of the graphene sheets disturbed the ordered structure of most graphene sheets [93]. Reviewing XRD patterns, the above results confirmed successful formation of SiO_2/CdSe -graphene with difference of CG and TEOS mass ratios as well as surfactant sources. Besides, achieved results promised that SCG nanocomposites were almost perfect, with single phase, high crystallinity, and high purity.

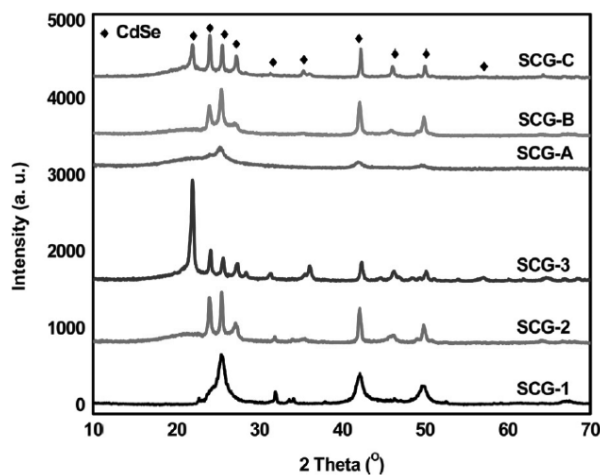


Fig. 8. XRD patterns of SiO_2/CdSe -graphene (SCG-1, SCG-2, SCG-3, SCG-A, SCG-B, and SCG-C) nanocomposites.

One of the key factors in evaluating physical properties is nitrogen adsorption/desorption isotherm that can provide a clear look at surface area determination and porosity analysis as well as characterization of pore volume, as well as the BET surface area, and pore size distribution derived from different survey nanocomposites. Results of nitrogen adsorption/desorption isotherms and pore size distributions, as well as corresponding textural parameters, are shown in Fig. 9 and Table 1. Considering the case of using CTAB as the surfactant template (SCG-1, SCG-2, and SCG-3 samples, Fig. 9(a), nitrogen adsorption-desorption isotherms of obtained nanocomposites at mass ratio of 5:100, and 10:100 are of type-IV curve and present the hysteresis loop in the relative pressure region around 0.40–1.0 p/p_0 , silica and CG combinations in SCG-1 and SCG-2 nanocomposites possessed a highly ordered mesoporous structure [34]. Correspondingly, pore size distribution calculated using the BJH method with existence of mesoporous structure in the composite (Table 1) of SCG-1 and SCG-2 reveals same narrow pore distribution with same value of 3.77/ nm. Main differences of SCG-1 and SCG-2 were displayed in the BET surface area and total pore volume factors. The BET surface area of SCG-1 prepared under mass ratio of 5:100 was 310.68 m^2/g , 2.7 times more than that of SCG-2 (113.69/ m^2/g), accompanied with total pore volume of SCG-1 also exhibited good results than SCG-2 with values were 71.38, and 26.12/ cm^3/g , respectively. Conversely, when mass ratios were increased to 15:100 (SCG-3), nitrogen

adsorption/desorption isotherm results of the SCG-3 nanocomposite clearly exhibit a similar type II curve. The BET surface area (11.33/ m^2/g), total pore volume (2.60/ cm^3/g), and pore size distribution (90.22/ nm) were obtained. In comparison, SCG-1 nanocomposite had a larger pore size, as well as a larger achieved specific surface area than others implies that SCG-1 is the best catalyst synthesized under the same surfactant template (CTAB) and the difference of TEOS and CG mass ratio.

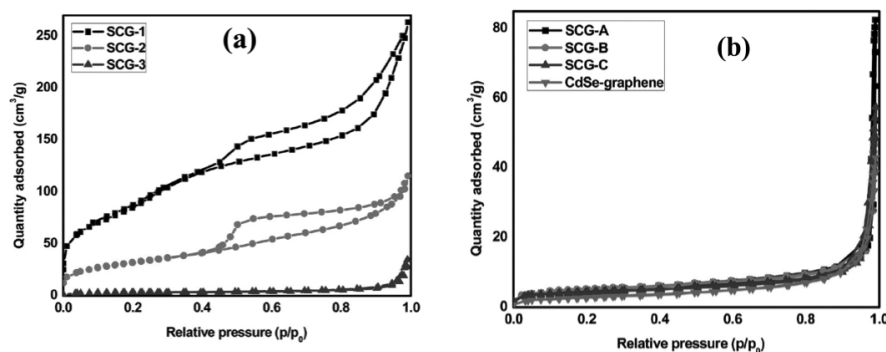


Fig. 9. Nitrogen adsorption/desorption isotherms for SiO₂/CdSe-graphene (SCG-1, SCG-2, SCG-3, SCG-A, SCG-B and SCG-C) and CdSe-graphene nanocomposites.

Table 1. Structure parameters of survey composites.

Sample	BET (m^2/g)	Total pore volume ($\text{cm}^3 \text{g}^{-1}$)	Average pore size (nm)
SCG-1	310.68	71.38	3.77
SCG-2	113.69	26.12	3.77
SCG-3	11.33	2.60	9.22
SCG-A	17.85	4.10	103.54
SCG-A	17.85	4.11	90.22
SCG-A	15.46	3.55	76.49
CdSe-graphene	10.65	2.45	66.74

On other aspects, in the case using SLS as the surfactant template (SCG-A, SCG-B, and SCG-C samples) and CG nanocomposites case, nitrogen adsorption-desorption isotherms of obtained nanocomposites at all mass ratio are of a type II curve with no hysteresis loop. According to Fig. 9(b), CG nanocomposite revealed small values of BET surface area, total pore volume, and average pore size was 10.65/ m^2/g , and 2.45/ cm^3/g , 66.74/ nm , respectively. Besides, the series of SiO₂/CdSe-graphene composite with SLS surfactant displayed higher values of BET surface area and total pore volume than CG composites, in region 15.46-17.85/ m^2/g , and 3.55-4.10/ cm^3/g , respectively. However, in the case of average pore size, pore size value of SiO₂/CdSe-graphene nanocomposite decreased with increased CG and TEOS mass ratios with 103.54, 90.22, 76.49/ nm corresponding to SCG-A, SCG-B and SCG-C nanocomposites. From obtained

results, there are two noteworthy points. First, the surfactant source has key influence on formation of material structure [35]. Corporeality, the mesoporous silica structure could be formed from raw material under the structure creator of CTAB at suitable experimental conditions. In our research, with CG and TEOS mass ratios of 5:100 and using CTAB as the template for formation of mesoporous material, achieved nanomaterials exhibited good physical properties. Replaced CTAB with SLS, the SiO_2/CdSe -graphene revealed no hysteresis loop in nitrogen adsorption/desorption isotherm that confirmed the solid structure of survey nanocomposites [[36], [37], [38], [39], [40]]. Second, mass ratio of raw materials plays a crucial role in formation of mesoporous silica structure as well as causing a certain influence in controlling development of the surface area, pore volume, and pore size distribution. From the difference of CG and TEOS mass ratio, we can achieve different results of physical properties such as surface area determination and porosity analysis. It is noted that the SCG-1 nanocomposite with larger pore size, and larger achieved specific surface area than others offers the promise of becoming a new potential material for the catalyst application field with high photocatalytic activity.

H_2 generation performance using $\text{g-C}_3\text{N}_4$ can be promoted with noble-metal particles such as Au or Pd, which obtain electrons in the CB to inhibit the charge recombination rate [86-90].

Many researchers are developing metal-free photocatalysts for H_2 evolution, and recent reports involved the introduction of non-noble-metal catalysts into $\text{g-C}_3\text{N}_4$ photocatalysts, displaying enhanced photocatalytic performance compared to noble-metal catalysts [91-95]. Hou et al. [86] synthesized $\text{MoS}_2/\text{g-C}_3\text{N}_4$ composite photocatalysts (Fig.10) in 2018. $\text{MoS}_2/\text{g-C}_3\text{N}_4$ increased the surface area and decreased the barrier when the electrons transported, thereby improving the charge transfer rate. The formation of band alignment enabled electron transfer from the CB ($\text{g-C}_3\text{N}_4$) to MoS_2 . Therefore, the $\text{MoS}_2/\text{g-C}_3\text{N}_4$ nano-junction significantly enhanced H_2 evolution efficiency, achieving the highest H_2 evolution rate and an optimum quantum efficiency of up to 2.1% (420 nm), which was higher than $\text{g-C}_3\text{N}_4/\text{Pt}$.

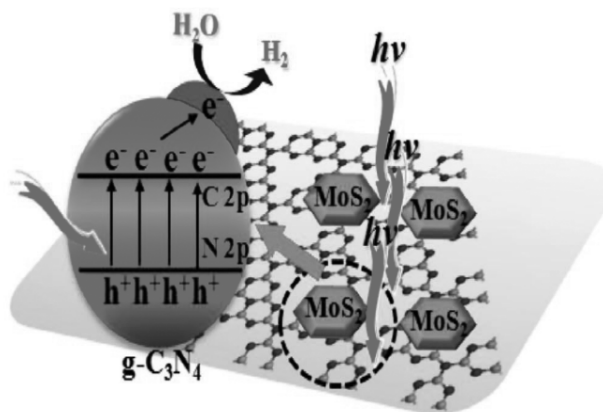


Fig. 10. Schematic display of charge transfer on $\text{MoS}_2/\text{g-C}_3\text{N}_4$ heterostructures during water splitting

Photocatalytic hydrogen production studies

Under ambient conditions, photocatalytic hydrogen evolution of as-synthesized nanocomposites was conducted to prove evidence of the ability to convert sunlight energy into chemical energy with/without sacrificial material [72]. In our research, methanol was used as the sacrificial reagent that can enable enhancement of catalytic capacity of the survey semiconductor through supplication electrons to consume photogenerated holes. And so, recombination time of semiconductor can be improved.

Results of hydrogen evolution are presented in Fig. 11. Among as-prepared composites, CG catalyst exhibited lowest H_2 evolution rate for both cases with/without presence of 20% methanol as a sacrificial reagent. There was only slight difference in this case with photocatalytic H_2 evolution rate were 0.98 and 1.19/ mmol/ 10/ h in pure water and methanol 20% sacrificing reagents under visible light irradiation, respectively. This is worth mentioning here is that the most photocatalytic hydrogen evolution capacity belongs to SCG-1 nano-composite. The SCG-C nano-composite ranked second that reached H_2 evolution rate from pure aqueous solution was 1.27/ mmol/ 10/ h, while it was 1.96/ mmol/ 10/ h in methanol 20% sacrificing reagents under visible light irradiation. Remarkable of all is photocatalytic H_2 evolution rate of the SCG-1 nano-composite that obtained approximately 1.8/ mmol/ 10/ h for the case of pure water and 3.35/ mmol/ 10/ h under presence of methanol 20% sacrificing reagents. Under presence of methanol 20%, H_2 evolution rate of SCG-1 was 1.7–2.8 times higher than that of SCG-C, and CG nano-composites.

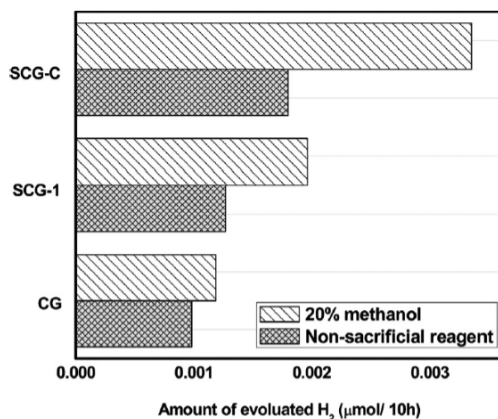


Fig. 11. Hydrogen production rate from pure water and an aqueous solution containing 20% methanol with SCG-C, SCG-1 and CG nanocomposites as photocatalysts.

Conclusion

Photocatalytic water splitting using semiconductor photocatalysts is a potentially promising technology for the production of renewable hydrogen energy via utilizing abundant solar light. Over the last decade or so, a number of studies were conducted to develop semiconductor photocatalysts that can efficiently use visible light for hydrogen

production. Several recent achievements demonstrated that the impact of factors such as preparation routes, photocatalytic conditions and the reasonable stability for commercialization. Though those materials are great for proof of concept studies, their efficiencies have repeatedly come up short. Therefore, another option would be to develop new materials and composites, either from promising new studies in literature, including some materials reviewed here, or with the aid of computational work. Modeling and mechanistic studies are of huge importance moving forward and can be extremely challenging.

References

- [1]. Park, S.J.; Lee, S.Y. A study on hydrogen-storage behaviors of nickel-loaded mesoporous MCM-41. *J. Colloid Interface Sci.* **2010**, *346*, 194–198.
- [2]. Catapan, R.C.; Cancino, L.R.; Oliveira, A.A.M.; Schwarz, C.O.; Nitschke, H.; Frank, T. Potential for onboard hydrogen production in an direct injection ethanol fueled spark ignition engine with EGR. *Fuel* **2018**, *234*, 441–446.
- [3]. Im, J.S.; Park, S.-J.; Kim, T.; Lee, Y.-S. Hydrogen storage evaluation based on investigations of the catalytic properties of metal/metal oxides in electrospun carbon fibers. *Int. J. Hydrogen Energy* **2009**, *34*, 3382–3388.
- [4]. Park, S.-J.; Lee, S.-Y. Hydrogen storage behaviors of platinum-supported multi-walled carbon nanotubes. *Int. J. Hydrogen Energy* **2010**, *35*, 13048–13054. [CrossRef]
- [5]. Lee, S.-Y.; Park, S.-J. Effect of platinum doping of activated carbon on hydrogen storage behaviors of metal-organic frameworks-5. *Int. J. Hydrogen Energy* **2011**, *36*, 8381–8387.
- [6]. Baykara, S.Z. Hydrogen: A brief overview on its sources, production and environmental impact. *Int. J. Hydrogen Energy* **2018**, *43*, 10605–10614.
- [7]. Chen, M.; Cui, W.; Zhu, K.; Xie, Y.; Zhang, C.; Shen, W. Hydrogen-rich water alleviates aluminum-induced inhibition of root elongation in alfalfa via decreasing nitric oxide production. *J. Hazard. Mater.* **2014**, *267*, 40–47.
- [8]. Cui, W.; Gao, C.; Fang, P.; Lin, G.; Shen, W. Alleviation of cadmium toxicity in *Medicago sativa* by hydrogen-rich water. *J. Hazard. Mater.* **2013**, *260*, 715–724.
- [9]. Gao, Q.; Song, H.; Wang, X.T.; Liang, Y.; Xi, Y.J.; Gao, Y.; Guo, Q.J.; LeBaron, T.; Luo, Y.X.; Li, S.C.; et al. Molecular hydrogen increases resilience to stress in mice. *Sci. Rep.* **2017**, *7*, 9625.
- [10]. Giuliani, D.; Ottani, A.; Zaffe, D.; Galantucci, M.; Strinati, F.; Lodi, R.; Guarini, S. Hydrogen sulfide slows down progression of experimental Alzheimer’s disease by targeting multiple pathophysiological mechanisms. *Neurobiol. Learn. Mem.* **2013**, *104*, 82–91.
- [11]. Huang, C.S.; Kawamura, T.; Toyoda, Y.; Nakao, A. Recent advances in hydrogen research as a therapeutic medical gas. *Free Radic. Res.* **2010**, *44*, 971–982.
- [12]. Kumar, R.; Kumar, A.; Langstrom, B.; Darreh-Shori, T. Discovery of novel choline acetyltransferase inhibitors using structure-based virtual screening. *Sci. Rep.* **2017**, *7*, 16287.
- [13]. Li, J.; Wang, C.; Zhang, J.H.; Cai, J.M.; Cao, Y.P.; Sun, X.J. Hydrogen-rich saline improves memory function in a rat model of amyloid-beta-induced Alzheimer’s disease by reduction of oxidative stress. *Brain Res.* **2010**, *1328*, 152–161.
- [14]. Luo, Q.; Lin, Y.X.; Yang, P.P.; Wang, Y.; Qi, G.B.; Qiao, Z.Y.; Li, B.N.; Zhang, K.; Zhang, J.P.; Wang, L.; et al. A self-destructive nanosweeper that captures and clears amyloid beta-peptides. *Nat. Commun.* **2018**, *9*, 1802
- [15]. Nagata, K.; Nakashima-Kamimura, N.; Mikami, T.; Ohsawa, I.; Ohta, S. Consumption of molecular hydrogen prevents the stress-induced impairments in hippocampus-dependent learning tasks during chronic physical restraint in mice. *Neuropsychopharmacol. Off. Publ. Am. Coll. Neuropsychopharmacol.* **2009**, *34*, 501–508.

- [16]. Nakayama, M.; Itami, N.; Suzuki, H.; Hamada, H.; Yamamoto, R.; Tsunoda, K.; Osaka, N.; Nakano, H.; Maruyama, Y.; Kabayama, S.; et al. Novel haemodialysis (HD) treatment employing molecular hydrogen (H₂)-enriched dialysis solution improves prognosis of chronic dialysis patients: A prospective observational study. *Sci. Rep.* **2018**, *8*, 254.
- [17]. Nishimaki, K.; Asada, T.; Ohsawa, I.; Nakajima, E.; Ikejima, C.; Yokota, T.; Kamimura, N.; Ohta, S. Effects of Molecular Hydrogen Assessed by an Animal Model and a Randomized Clinical Study on Mild Cognitive Impairment. *Curr. Alzheimer Res.* **2018**, *15*, 482–492.
- [18]. Ohsawa, I.; Ishikawa, M.; Takahashi, K.; Watanabe, M.; Nishimaki, K.; Yamagata, K.; Katsura, K.; Katayama, Y.; Asoh, S.; Ohta, S. Hydrogen acts as a therapeutic antioxidant by selectively reducing cytotoxic oxygen radicals. *Nat. Med.* **2007**, *13*, 688–694.
- [19]. Xiao, H.W.; Li, Y.; Luo, D.; Dong, J.L.; Zhou, L.X.; Zhao, S.Y.; Zheng, Q.S.; Wang, H.C.; Cui, M.; Fan, S.J. Hydrogen-water ameliorates radiation-induced gastrointestinal toxicity via MyD88's effects on the gut microbiota. *Exp. Mol. Med.* **2018**, *50*, e433.
- [20]. Zhang, L.M.; Jiang, C.X.; Liu, D.W. Hydrogen sulfide attenuates neuronal injury induced by vascular dementia via inhibiting apoptosis in rats. *Neurochem. Res.* **2009**, *34*, 1984–1992.
- [21]. Zhang, Y.; Su, W.J.; Chen, Y.; Wu, T.Y.; Gong, H.; Shen, X.L.; Wang, Y.X.; Sun, X.J.; Jiang, C.L. Effects of hydrogen-rich water on depressive-like behavior in mice. *Sci. Rep.* **2016**, *6*, 23742.
- [22]. Liu, S.; Xin, Z.-J.; Lei, Y.-J.; Yang, Y.; Yan, X.-Y.; Lu, Y.-B.; Li, C.-B.; Wang, H.-Y. Thin Copper-Based Film for Efficient Electrochemical Hydrogen Production from Neutral Aqueous Solutions. *ACS Sustain. Chem. Eng.* **2017**, *5*, 7496–7501. [CrossRef]
- [23]. Wang, Z.; Yang, X.; Yang, T.; Zhao, Y.; Wang, F.; Chen, Y.; Zeng, J.H.; Yan, C.; Huang, F.; Jiang, J.-X. Dibenzo thiophene Dioxide Based Conjugated Microporous Polymers for Visible-Light-Driven Hydrogen Production. *ACS Catal.* **2018**, *8*, 8590–8596. [CrossRef]
- [24]. Zhu, K.; Kang, S.-Z.; Qin, L.; Han, S.; Li, G.; Li, X. Novel and Highly Active Potassium Niobate-Based Photocatalyst for Dramatically Enhanced Hydrogen Production. *J. Am. Chem. Soc.* **2005**, *127*, 11447–11453. [CrossRef]
- [25]. Hibino, T.; Kobayashi, K.; Ito, M.; Ma, Q.; Nagao, M.; Fukui, M.; Teranishi, S. Kinetics of the Interconversion of Parahydrogen and Orthohydrogen Catalyzed by Paramagnetic Complex Ions. *J. Am. Chem. Soc.* **2005**, *127*, 11447–11453.
- [26]. Fujishima, A.; Honda, K. Electrochemical Photolysis of Water at a Semiconductor Electrode. *Nature* **1972**, *238*, 37–38.
- [27]. Zhang, P.; Song, T.; Wang, T.; Zeng, H. In-situ synthesis of Cu nanoparticles hybridized with carbon quantum dots as a broad spectrum photocatalyst for improvement of photocatalytic H₂ evolution. *Appl. Catal. B Environ.* **2017**, *206*, 328–335.
- [28]. Zhang, P.; Song, T.; Wang, T.; Zeng, H. Plasmonic Cu nanoparticle on reduced graphene oxide nanosheet support: An efficient photocatalyst for improvement of near-infrared photocatalytic H₂ evolution. *Appl. Catal. B Environ.* **2018**, *225*, 172–179. [CrossRef]
- [29]. Zhang, P.; Wang, T.; Zeng, H. Design of Cu-Cu₂O/g-C₃N₄ nanocomponent photocatalysts for hydrogen evolution under visible light irradiation using water-soluble Erythrosin B dye sensitization. *Appl. Surf. Sci.* **2017**, *391*, 404–414. [CrossRef]
- [30]. Zhang, P.; Song, T.; Wang, T.; Zeng, H. Effectively extending visible light absorption with a broad spectrum sensitizer for improving the H₂ evolution of in-situ Cu/g-C₃N₄ nanocomponents. *Int. J. Hydrogen Energy* **2017**, *42*, 14511–14521. [CrossRef]
- [31]. Zhang, Y.; Park, M.; Kim, H.Y.; Ding, B.; Park, S.J. A facile ultrasonic-assisted fabrication of nitrogen-doped carbon dots/BiOBr up-conversion nanocomposites for visible light photocatalytic enhancements. *Sci. Rep.* **2017**, *7*, 45086. [CrossRef] [PubMed]
- [32]. Zhang, Y.; Park, S.-J. Bimetallic AuPd alloy nanoparticles deposited on MoO₃ nanowires for enhanced visible-light driven trichloroethylene degradation. *J. Catal.* **2018**, *361*, 238–247. [CrossRef]

- [33]. Zhang, Y.; Park, S.-J. Au-pd bimetallic alloy nanoparticle-decorated BiPO₄ nanorods for enhanced photocatalytic oxidation of trichloroethylene. *J. Catal.* 2017, 355, 1–10.
- [34]. Yu, H.; Xue, Y.; Hui, L.; Zhang, C.; Li, Y.; Zuo, Z.; Zhao, Y.; Li, Z.; Li, Y. Efficient Hydrogen Production on 3D Flexible Heterojunction Material. *Adv. Mater.* 2018, 30, e1707082.
- [35]. Zhang, P.; Song, T.; Wang, T.; Zeng, H. Fabrication of a non-semiconductor photocatalytic system using dendrite-like plasmonic CuNi bimetal combined with a reduced graphene oxide nanosheet for near-infrared photocatalytic H₂ evolution. *J. Mater. Chem. A* 2017, 5, 22772–22781.
- [36]. Lin, L.; Ren, W.; Wang, C.; Asiri, A.M.; Zhang, J.; Wang, X. Crystalline carbon nitride semiconductors prepared at different temperatures for photocatalytic hydrogen production. *Appl. Catal. B Environ.* 2018, 231, 234–241.
- [37]. Im, J.S.; Kwon, O.; Kim, Y.H.; Park, S.-J.; Lee, Y.-S. The effect of embedded vanadium catalyst on activated electrospun CFs for hydrogen storage. *Microporous Mesoporous Mater.* 2008, 115, 514–521.
- [38]. Yi, H.; Huang, D.; Qin, L.; Zeng, G.; Lai, C.; Cheng, M.; Ye, S.; Song, B.; Ren, X.; Guo, X. Selective prepared carbon nanomaterials for advanced photocatalytic application in environmental pollutant treatment and hydrogen production. *Appl. Catal. B Environ.* 2018, 239, 408–424.
- [39]. Ismail, A.A.; Bahnemann, D.W. Photochemical splitting of water for hydrogen production by photocatalysis: A review. *Sol. Energy Mater. Sol. Cells* 2014, 128, 85–101.
- [40]. Cai, J.; Shen, J.; Zhang, X.; Ng, Y.H.; Huang, J.; Guo, W.; Lin, C.; Lai, Y. Light-Driven Sustainable Hydrogen Production Utilizing TiO₂ Nanostructures: A Review. *Small Methods* 2018, 1800184.
- [41]. Ventura-Espinosa, D.; Sabater, S.; Carretero-Cerdán, A.; Baya, M.; Mata, J.A. High Production of Hydrogen on Demand from Silanes Catalyzed by Iridium Complexes as a Versatile Hydrogen Storage System. *ACS Catal.* 2018, 8, 2558–2566.
- [42]. Ji, L.; Lv, C.; Chen, Z.; Huang, Z.; Zhang, C. Nickel-Based (Photo) Electrocatalysts for Hydrogen Production. *Adv. Mater.* 2018, 30, e1705653.
- [43]. Ma, Y.; Dong, X.; Wang, Y.; Xia, Y. Decoupling Hydrogen and Oxygen Production in Acidic Water Electrolysis Using a Polytriphenylamine-Based Battery Electrode. *Angewandte Chem.* 2018, 57, 2904–2908.
- [44]. Wang, B.; Zeng, C.; Chu, K.H.; Wu, D.; Yip, H.Y.; Ye, L.; Wong, P.K. Enhanced Biological Hydrogen Production from *Escherichia coli* with Surface Precipitated Cadmium Sulfide Nanoparticles. *Adv. Energy Mater.* 2017, 7, 1700611.
- [45]. Xue, Z.; Shen, Y.; Li, P.; Zhang, Y.; Li, J.; Qin, B.; Zhang, J.; Zeng, Y.; Zhu, S. Key Role of Lanthanum Oxychloride: Promotional Effects of Lanthanum in NiLaO_y/NaCl for Hydrogen Production from Ethyl Acetate and Water. *Small* 2018, 14, e1800927.
- [46]. Zhang, Y.; Yang, H.M.; Park, S.-J. Synthesis and characterization of nitrogen-doped TiO₂ coatings on reduced graphene oxide for enhancing the visible light photocatalytic activity. *Curr. Appl. Phys.* 2018, 18, 163–169.
- [47]. Zhang, Y.; Park, M.; Kim, H.-Y.; Park, S.-J. In-situ synthesis of graphene oxide/BiOCl heterostructured nanofibers for visible-light photocatalytic investigation. *J. Alloy Compd.* 2016, 686, 106–114.
- [48]. Huang, J.; Li, G.; Zhou, Z.; Jiang, Y.; Hu, Q.; Xue, C.; Guo, W. Efficient photocatalytic hydrogen production over Rh and Nb codoped TiO₂ nanorods. *Chem. Eng. J.* 2018, 337, 282–289.
- [49]. Kim, W.; Monllor-Satoca, D.; Chae, W.-S.; Mahadik, M.A.; Jang, J.S. Enhanced photoelectrochemical and hydrogen production activity of aligned CdS nanowire with anisotropic transport properties. *Appl. Surf. Sci.* 2019, 463, 339–347.
- [50]. Han, J.; Liu, Y.; Dai, F.; Zhao, R.; Wang, L. Fabrication of CdSe/CaTiO₃ nanocomposites in aqueous solution for improved photocatalytic hydrogen production. *Appl. Surf. Sci.* 2018, 459, 520–526.
- [51]. Zhang, Y.; Park, M.; Kim, H.Y.; Ding, B.; Park, S.-J. In-situ synthesis of nanofibers with various ratios of BiOCl_x/BiOBry/BiOIz for effective trichloroethylene photocatalytic degradation. *Appl. Surf. Sci.*

- 2016, 384, 192–199.
- [52]. Pipitone, G.; Tosches, D.; Bensaid, S.; Galia, A.; Pirone, R. Valorization of alginate for the production of hydrogen via catalytic aqueous phase reforming. *Catal. Today* 2018, 304, 153–164.
- [53]. Hibino, T.; Kobayashi, K.; Ito, M.; Nagao, M.; Fukui, M.; Teranishi, S. Direct electrolysis of waste newspaper for sustainable hydrogen production: An oxygen-functionalized porous carbon anode. *Appl. Catal. B Environ.* 2018, 231, 191–199.
- [54]. Park, S.; Kim, B.; Lee, Y.; Cho, M. Influence of copper electroplating on high pressure hydrogen-storage behaviors of activated carbon fibers. *Int. J. Hydrogen Energy* 2008, 33, 1706–1710.
- [55]. Im, J.S.; Park, S.-J.; Lee, Y.-S. Superior prospect of chemically activated electrospun carbon fibers for hydrogen storage. *Mater. Res. Bull.* 2009, 44, 1871–1878.
- [56]. Xiang, Q.; Yu, J. Graphene-Based Photocatalysts for Hydrogen Generation. *J. Phys. Chem. Lett.* 2013, 4, 753–759.
- [57]. Kim, H.-I.; Moon, G.-H.; Monllor-Satoca, D.; Park, Y.; Choi, W. Solar Photoconversion Using Graphene/TiO₂ Composites: Nanographene Shell on TiO₂ Core versus TiO₂ Nanoparticles on Graphene Sheet. *J. Phys. Chem. C* 2011, 116, 1535–1543.
- [58]. Wu, Z.; Zhou, Z.; Zhang, Y.; Wang, J.; Shi, H.; Shen, Q.; Wei, G.; Zhao, G. Simultaneous photoelectrocatalytic aromatic organic pollutants oxidation for hydrogen production promotion with a self-biasing photoelectrochemical cell. *Électrochim. Acta* 2017, 254, 140–147.
- [59]. Kim, B.J.; Lee, Y.S.; Park, S.J. Preparation of platinum-decorated porous graphite nanofibers, and their hydrogen storage behaviors. *J. Colloid Interface Sci.* 2008, 318, 530–533.
- [60]. Zhang, Y.; Park, S.-J. Fabrication and characterization of flower-like BiOI/Pt heterostructure with enhanced photocatalytic activity under visible light irradiation. *J. Solid State Chem.* 2017, 253, 421–429.
- [61]. Zhang, Y.; Park, S.-J. Incorporation of RuO₂ into charcoal-derived carbon with controllable microporosity by CO₂ activation for high-performance supercapacitor. *Carbon* 2017, 122, 287–297.
- [62]. Panthi, G.; Park, M.; Kim, H.-Y.; Park, S.-J. Electrospun polymeric nanofibers encapsulated with nanostructured materials and their applications: A review. *J. Ind. Eng. Chem.* 2015, 24, 1–13.
- [63]. Panthi, G.; Park, M.; Kim, H.-Y.; Lee, S.-Y.; Park, S.-J. Electrospun ZnO hybrid nanofibers for photodegradation of wastewater containing organic dyes: A review. *J. Ind. Eng. Chem.* 2015, 21, 26–35.
- [64]. Kim, S.; Park, S. Electroactivity of Pt-Ru/polyaniline composite catalyst-electrodes prepared by electrochemical deposition methods. *Solid State Ion.* 2008, 178, 1915–1921.
- [65]. Park, S.J.; Kim, B.J. Influence of oxygen plasma treatment on hydrogen chloride removal of activated carbon fibers. *J. Colloid Interface Sci.* 2004, 275, 590–595.
- [66]. Park, S.-J.; Kim, J.S. Modifications produced by electrochemical treatments on carbon blacks. Microstructures and mechanical interfacial properties. *Carbon* 2001, 39, 2011–2016.
- [67]. Chen, W.-T.; Chan, A.; Sun-Waterhouse, D.; Llorca, J.; Idriss, H.; Waterhouse, G.I.N. Performance comparison of Ni/TiO₂ and Au/TiO₂ photocatalysts for H₂ production in different alcohol-water mixtures. *J. Catal.* 2018, 367, 27–42.
- [68]. Hou, H.; Liu, H.; Gao, F.; Shang, M.; Wang, L.; Xu, L.; Wong, W.-Y.; Yang, W. Packaging BiVO₄ nanoparticles in ZnO microbelts for efficient photoelectrochemical hydrogen production. *Electrochim. Acta* 2018, 283, 497–508.
- [69]. Belhadj, H.; Hamid, S.; Robertson, P.K.J.; Bahnemann, D.W. Mechanisms of Simultaneous Hydrogen Production and Formaldehyde Oxidation in H₂O and D₂O over Platinized TiO₂. *ACS Catal.* 2017, 7, 4753–4758.
- [70]. Akbarzadeh, R.; Ghaedi, M.; Nasiri Kokhdan, S.; Jannesar, R.; Sadeghfar, F.; Sadri, F.; Tayebi, L. Electrochemical hydrogen storage, photocatalytic and antibacterial activity of Fe Ag bimetallic nanoparticles supported on TiO₂ nanowires. *Int. J. Hydrogen Energy* 2018, 43, 18316–18329.
- [71]. Chen, C.; Cai, W.M.; Long, M.C.; Zhou, B.X.; Wu, Y.H.; Wu, D.Y.; Feng, Y.J. Synthesis of Visible Light

- Responsive Graphene Oxide/ TiO₂ Composites with p/n Heterojunction. *ACS Nano* 2010, 4, 6425–6432.
- [72]. Cao, S.; Yu, J. g-C₃N₄-Based Photocatalysts for Hydrogen Generation. *J. Phys. Chem. Lett.* 2014, 5, 2101–2107.
- [73]. Rather, R.A.; Singh, S.; Pal, B. A C₃N₄ surface passivated highly photoactive Au-TiO₂ tubular nanostructure for the efficient H₂ production from water under sunlight irradiation. *Appl. Catal. B Environ.* 2017, 213, 9–17.
- [74]. Bian, H.; Ji, Y.; Yan, J.; Li, P.; Li, L.; Li, Y.; Frank Liu, S. In Situ Synthesis of Few-Layered g-C₃N₄ with Vertically Aligned MoS₂ Loading for Boosting Solar-to-Hydrogen Generation. *Small* 2018, 14, 1703003.
- [75]. Tian, N.; Zhang, Y.; Li, X.; Xiao, K.; Du, X.; Dong, F.; Waterhouse, G.I.N.; Zhang, T.; Huang, H. Precursor-reforming protocol to 3D mesoporous g-C₃N₄ established by ultrathin self-doped nanosheets for superior hydrogen evolution. *Nano Energy* 2017, 38, 72–81.
- [76]. Xu, X.; Si, Z.; Liu, L.; Wang, Z.; Chen, Z.; Ran, R.; He, Y.; Weng, D. CoMoS₂/rGO/C₃N₄ ternary heterojunctions catalysts with high photocatalytic activity and stability for hydrogen evolution under visible light irradiation. *Appl. Surf. Sci.* 2018, 435, 1296–1306.
- [77]. Luo, X.; Wu, Z.; Liu, Y.; Ding, S.; Zheng, Y.; Jiang, Q.; Zhou, T.; Hu, J. Engineering Amorphous Carbon onto Ultrathin g-C₃N₄ to Suppress Intersystem Crossing for Efficient Photocatalytic H₂ Evolution. *Adv. Mater. Interfaces* 2018, 5, 1800859.
- [78]. Wang, Y.; Wang, X.; Antonietti, M. Polymeric graphitic carbon nitride as a heterogeneous organocatalyst: From photochemistry to multipurpose catalysis to sustainable chemistry. *Angewandte Chem.* 2012, 51, 68–89.
- [79]. Wang, X.; Maeda, K.; Thomas, A.; Takanabe, K.; Xin, G.; Carlsson, J.M.; Domen, K.; Antonietti, M. A metal-free polymeric photocatalyst for hydrogen production from water under visible light. *Nat. Mater.* 2009, 8, 76–80.
- [80]. Gao, H.; Yang, H.; Xu, J.; Zhang, S.; Li, J. Strongly Coupled g-C₃N₄ Nanosheets-Co₃O₄ Quantum Dots as 2D/0D Heterostructure Composite for Peroxymonosulfate Activation. *Small* 2018, 14, 1801353.
- [81]. Chen, Z.; Xia, K.; She, X.; Mo, Z.; Zhao, S.; Yi, J.; Xu, Y.; Chen, H.; Xu, H.; Li, H. 1D metallic MoO₂-C as co-catalyst on 2D g-C₃N₄ semiconductor to promote photocatalytic hydrogen production. *Appl. Surf. Sci.* 2018, 447, 732–739.
- [82]. Kong, L.; Ji, Y.; Dang, Z.; Yan, J.; Li, P.; Li, Y.; Liu, S.F. g-C₃N₄ Loading Black Phosphorus Quantum Dot for Efficient and Stable Photocatalytic H₂ Generation under Visible Light. *Adv. Funct. Mater.* 2018, 28, 1800668.
- [83]. Wan, J.; Pu, C.; Wang, R.; Liu, E.; Du, X.; Bai, X.; Fan, J.; Hu, X. A facile dissolution strategy facilitated by H₂SO₄ to fabricate a 2D metal-free g-C₃N₄/rGO heterojunction for efficient photocatalytic H₂ production. *Int. J. Hydrogen Energy* 2018, 43, 7007–7019.
- [84]. Marcì, G.; García-López, E.I.; Palmisano, L. Polymeric carbon nitride (C₃N₄) as heterogeneous photocatalyst for selective oxidation of alcohols to aldehydes. *Catal. Today* 2018, 315, 126–137.
- [85]. Oh, W.-D.; Lok, L.-W.; Veksha, A.; Giannis, A.; Lim, T.-T. Enhanced photocatalytic degradation of bisphenol A with Ag-decorated S-doped g-C₃N₄ under solar irradiation: Performance and mechanistic studies. *Chem. Eng. J.* 2018, 333, 739–749.
- [86]. Zhang, Y.; Park, S.-J. Facile construction of MoO₃@ZIF-8 core-shell nanorods for efficient photoreduction of aqueous Cr (VI). *Appl. Catal. B Environ.* 2019, 240, 92–101.
- [87]. Kamijyo, K.; Takashima, T.; Yoda, M.; Osaki, J.; Irie, H. Facile synthesis of a red light-inducible overall water-splitting photocatalyst using gold as a solid-state electron mediator. *Chem. Commun.* 2018, 54, 7999–8002.
- [88]. Maeda, K.; Domen, K. Photocatalytic Water Splitting: Recent Progress and Future Challenges. *J. Phys. Chem. Lett.* 2010, 1, 2655–2661.
- [89] A.E. Raevskaya, A.L. Stroyuk, S.Y. Kuchmiy, et al., Growth and spectroscopic characterization of

- CdSe nanoparticles synthesized from CdCl₂ and Na₂SeSO₃ in aqueous gelatin solutions, *Colloids Surf. A* 290 (1–3) (2006) 304–309.
- [90] T. Wang, J. Wang, Y. Zhu, F. Xue, J. Cao, Y. Qian, Solvothermal synthesis and characterization of CdSe nanocrystals with controllable phase and morphology, *J. Phys. Chem. Solids* 71 (7) (2010) 940–945.
- [91] X.M. Guo, X.G. Liu, B.S. Xu, et al., Synthesis and characterization of carbon spheresilica core-shell structure and hollow silica spheres, *Colloids Surf. A* 345 (2009) 141–146.
- [92] Wen Ling Zhang, Hyoung Jin Choi, Silica-graphene oxide hybrid composite particles and their electroresponsive characteristics, *Langmuir* 28 (17) (2012) 7055–7062.
- [93] Dinh Cung Tien Nguyen, Kwang-Youn Cho, Oh Won-Chun, Synthesis of mesoporous SiO₂/Cu₂O-graphene nanocomposites and their highly efficient photocatalytic performance for dye pollutants, *RSC Adv.* 7 (2017) 29284–29294.



This document was created with the Win2PDF "print to PDF" printer available at <http://www.win2pdf.com>

This version of Win2PDF 10 is for evaluation and non-commercial use only.

This page will not be added after purchasing Win2PDF.

<http://www.win2pdf.com/purchase/>